



Miscible viscous fingering in a packed cylindrical column: Theory and numerics

Min Chan Kim ^{1,*} and Satyajit Pramanik ^{2,†}¹*Department of Chemical Engineering, Jeju National University, Jeju 63243, Republic of Korea*²*Department of Mathematics, Indian Institute of Technology Guwahati, Guwahati 781039, Assam, India*

(Received 24 August 2021; accepted 23 November 2022; published 17 January 2023)

We investigate viscous fingering (VF) during the miscible displacement in a cylindrical packed column using linear stability analysis and numerical solutions. Linear stability theory is carried out in a self-similar domain, and the linearized equations are solved with and without the quasi-steady-state approximation. We obtain the onset of instability and the associated critical parameters as functions of the log-viscosity ratio and Péclet number for the onset of instability using linear stability analysis. Further, we perform nonlinear simulations based on the finite-element method, both in two- and three-dimensional domains. It is shown that the critical Péclet numbers obtained from the linear and nonlinear analyses are in good agreement. One of the main objectives of this study is to explore the effects of lateral boundary conditions on VF. Through two-dimensional (2D) and three-dimensional (3D) simulations, we have clearly shown that the onset and the growth of VF are strongly dependent on the lateral boundary conditions. Finally, through our present 3D numerical simulations, we successfully produce the experimental results available in the literature by suitably choosing the parameters that replicate the experimental conditions under consideration.

DOI: [10.1103/PhysRevFluids.8.013901](https://doi.org/10.1103/PhysRevFluids.8.013901)

I. INTRODUCTION

When a less viscous fluid displaces a more viscous defending fluid in a porous medium, the fluid-fluid interface becomes hydrodynamically unstable and fingerlike patterns are formed at the interface. This instability, which is known as viscous fingering (VF), is a fundamental fluid mechanics problem that is relevant to secondary oil recovery, channeling in packed bed column, fixed bed regeneration, etc. [1]. Using an x-ray technique, Slobod *et al.* [2] and Perkins *et al.* [3] experimentally analyzed the onset and the evolution of the miscible fingering. They showed that at high flow rates, fingers are present near the injection region, while no fingers are observed near the injection region at low flow rates. These experimental results indicate that the stability characteristics are influenced by the viscosity profile and the flow rate. Therefore, there is a stable region even if the viscosity distribution is unfavorable.

Due to the richness in fundamental aspects as well as a wide range of applications, numerous theoretical and numerical studies have been conducted on VF by researchers in a wide range of settings ([4–15] and references therein). Nonlinear fingering dynamics such as tip splitting, merging, and mixing of a finite sample were investigated numerically [16]. Pramanik *et al.* [6] extended this idea for a circular sample and showed that along with the viscous fingering instability, two more instability patterns were formed in this case, unlike a finite sample. Particle-induced viscous fingering was investigated experimentally by modifying the effective viscosity of the displacing and

*mckim@cheju.ac.kr

†satyajitp@iitg.ac.in

the defending fluids [7]. Critical dependences of viscous fingering on the inlet boundary condition were reported using linear stability analysis and nonlinear simulations [10]. Gao *et al.* [11] showed that the electric field can be used to control viscous fingering in a Hele-Shaw cell. Incorporating nonlinear adsorption of the Langmuir type in the model of De Wit *et al.* [16] and Rana *et al.* [12] showed that adsorption parameters can be efficiently used to viscous fingering instability in a liquid chromatographic condition. Nonmodal stability analysis of viscous fingering was used to capture transient growth in a two-dimensional setting [17]. Reference [13] extended the finite sample viscous fingering model in a radial geometry and showed that the fingering instability depends both on the size of the sample and the location of the sample in the Hele-Shaw cell. Linear stability analysis and nonlinear simulations showed that a chemical reaction can also be used as a control parameter of VF in a radial geometry [18,19].

Pramanik and Mishra [20] investigated the effects of the Péclet number, Pe , in a two-dimensional domain with no-flux conditions at the lateral boundaries using linear stability analysis and nonlinear numerical simulations. Recently, Nijjer *et al.* [21] studied the full life cycle of miscible VF, from the onset to shutdown, using periodic boundary conditions in a two-dimensional flow.

Experimental studies of miscible VF in liquid chromatographic conditions revealed that for samples of low viscosity, fingering might not be observed in short chromatographic columns and the velocity at which the sample is displaced influences the onset and evolution of fingering [22,23]. Recently, Suekane *et al.* [24] studied the onset and the three-dimensional growth of viscous fingering in a cylindrical column using an x-ray computerized tomographic technique. Rousseaux *et al.* [25] conducted a theoretical analysis based on the quasi-steady-state approximation (QSSA) to analyze VF in liquid chromatography columns.

The above-mentioned theoretical and computational studies provide useful insights about miscible VF in porous media. However, these studies considered two-dimensional flows without including any physical lateral boundaries. Therefore, these results are not directly applicable to liquid chromatographic conditions, which is a three-dimensional flow configuration confined by a physical lateral boundary. The lateral boundary effects on VF in a capillary tube were analyzed by Chen and Meiburg [26,27]. However, these studies have their demerits in explaining a three-dimensional liquid chromatography column as they restrict their analyses to axisymmetric two-dimensional domains.

In the present study, the onset of viscous fingering during the miscible displacement in a three-dimensional cylindrical packed column is analyzed theoretically and numerically. Under the linear stability theory, the stability equations are derived and reformulated in the cylindrical coordinate system to consider radial boundary effects. These stability equations are transformed in terms of self-similar coordinates and are solved analytically and numerically. Further, for some extreme cases, the stability characteristics are obtained without the aid of the QSSA. Thus, the present study might be useful to understand the validity and limitation of the QSSA. To study the nonlinear growth of the instability motion, we perform nonlinear numerical simulations. The present theoretical and numerical results show good agreement and explain the previous experimental finding.

II. MATHEMATICAL MODEL AND BASE STATE

Governing equations and base fields

We consider uniform miscible displacement in a packed cylindrical column of radius b as schematized in Fig. 1. The fluids are Newtonian and neutrally buoyant, and the porous media is homogeneous with a constant permeability and isotropic dispersion. Using Darcy's law, the governing equation for the present system can be written as [4,21]

$$\nabla \cdot \mathbf{U} = 0, \quad (1a)$$

$$\frac{\mu}{\kappa} \mathbf{U} = -\nabla P, \quad (1b)$$

$$\varepsilon \frac{\partial C}{\partial t} + \mathbf{U} \cdot \nabla C = D \nabla^2 C, \quad (1c)$$

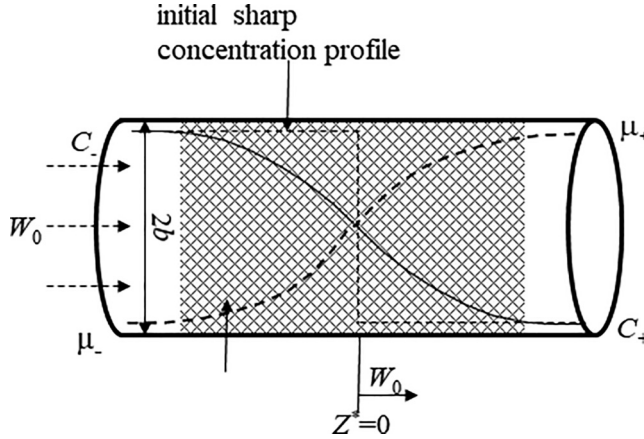


FIG. 1. Schematic diagram of the system considered here.

where \mathbf{U} is the velocity vector, μ the viscosity, ε the porosity, κ the permeability, P the pressure, C the concentration of solvent, and D the dispersion coefficient, which is assumed constant and isotropic. By considering the displacing motion with the uniform velocity W_0 , a moving reference frame $Z^* = Z - W_0 t$ is adopted and the above governing equation can be written in dimensionless form as

$$\nabla \cdot \mathbf{u} = 0, \quad (2a)$$

$$\bar{\mu}(\mathbf{u} + \mathbf{i}) = -\nabla p, \quad (2b)$$

$$\frac{\partial c}{\partial \tau} + \mathbf{u} \cdot \nabla c = \frac{1}{\text{Pe}} \nabla^2 c, \quad (2c)$$

using b , b/W_0 , W_0 , μ_- , $\mu_- W_0 b/k$, and $\Delta C = C_- - C_+$ as the length, time, velocity, viscosity, pressure, and concentration scales, respectively. Here, μ_- , C_- , and C_+ are the viscosity of the displaced fluid, and the solute concentration for the displacing and displaced fluid, respectively. Further, $\bar{\mu} = \mu/\mu_-$, $\text{Pe} = W_0 b/D$ is the Péclet number and \mathbf{i} is the unit vector in the displacing direction.

In the moving reference frame, we have $\mathbf{u}_0 = \mathbf{0}$, and hence the base state concentration is described by the diffusion equation,

$$\frac{\partial c_0}{\partial \tau} = \frac{1}{\text{Pe}} \frac{\partial^2 c_0}{\partial z^2}, \quad (3)$$

subject to the initial and boundary conditions,

$$c_0(0, z) = 1 - H(z), \quad (4a)$$

$$1 - c_0(\tau, -\infty) = c_0(\tau, \infty) = 0, \quad (4b)$$

where $H(z)$ is the Heaviside step function. From Eqs. (3) and (4), the base concentration field can be expressed as

$$c_0 = \frac{1}{2} \text{erfc} \left(\frac{\xi \sqrt{\text{Pe}}}{2} \right), \quad (5)$$

where $\xi = z/\sqrt{\tau}$ is the similarity variable.

III. LINEAR STABILITY ANALYSIS

Stability analysis

Eliminating pressure and the spanwise velocity from Eqs. (2), and linearizing the resultant equations in terms of the perturbation to the concentration and streamwise velocity, we obtain

$$\nabla^2 w_1 + \frac{1}{\bar{\mu}} \frac{\partial \bar{\mu}}{\partial z} = \frac{1}{\bar{\mu}} \frac{\partial \bar{\mu}}{\partial c_0} \nabla_1^2 c_1, \quad (6a)$$

$$\frac{\partial c_1}{\partial \tau} + \frac{\partial c_0}{\partial z} w_1 = \frac{1}{\text{Pe}} \nabla^2 c_1, \quad (6b)$$

where $\nabla^2 = \frac{\partial^2}{\partial z^2} + \nabla_1^2$ and $\nabla_1^2 = \frac{1}{r} \frac{\partial}{\partial r} (r \frac{\partial}{\partial r}) + \frac{1}{r^2} \frac{\partial^2}{\partial \theta^2}$. The associated boundary conditions are given by

$$w_1 \rightarrow 0 \text{ and } c_1 \rightarrow 0 \text{ as } z \rightarrow \pm\infty, \quad (7a)$$

$$\frac{\partial w_1}{\partial r} = \frac{\partial c_1}{\partial r} = 0 \text{ at } r = 0 \text{ and } 1. \quad (7b)$$

In the present study, following Tan and Homsy [4], we arrive at the linear stability equation (6) from the governing equation (2). Furthermore, the symmetry conditions at $r = 0$ are equivalent to the finite condition, i.e., $w_1 = \text{finite}$ and $c_1 = \text{finite}$ at $r = 0$ [28].

Following Wooding [28], under the normal mode analysis, the disturbance quantities are decomposed as

$$[w_1, c_1] = [\bar{w}_1(\tau, z), \bar{c}_1(\tau, z)] X_l^m(r, \theta). \quad (8)$$

The cylindrical harmonics $X_l^m(r, \theta)$ can completely determine the horizontal dependency of the disturbance quantities through the following relation:

$$\nabla_1^2 X_l^m = -\alpha_{l,m}^2 X_l^m, \quad (9)$$

where

$$X_l^m(r, \theta) = J_m(\alpha_{l,m} r) \exp(im\theta), \quad m = 0, 1, 2, \dots, \quad (10)$$

and

$$J'_m(\alpha_{l,m}) = 0, \quad l = 1, 2, 3, \dots, \quad (11)$$

where J_m is the Bessel's function of the first kind, $\alpha_{l,m}$ is the eigenvalue, and $i = \sqrt{-1}$. A few zeros of Eq. (11) are summarized in Fig. 2. The nonaxisymmetric case of $m > 0$ satisfies the continuity requirement through the factor $\exp(im\theta)$ and the axisymmetric one of $m = 0$ also does through the integral over the cylinder cross section as

$$\int_0^1 r J_0(\alpha_{l,0}, r) dr = \frac{J_1(\alpha_{l,0})}{\alpha_{l,0}} = 0, \quad (12)$$

by using the zeros of Eq. (11) [28]. Therefore, the stability equations become

$$\left(\frac{\partial^2}{\partial z^2} + \frac{1}{\bar{\mu}} \frac{\partial \bar{\mu}}{\partial z} \frac{\partial}{\partial z} - \alpha_{l,m}^2 \right) \bar{w}_1 = -\frac{1}{\bar{\mu}} \frac{\partial \bar{\mu}}{\partial c_0} \alpha_{l,m}^2 \bar{c}_1, \quad (13a)$$

$$\frac{\partial \bar{c}_1}{\partial \tau} + \bar{w}_1 \frac{\partial c_0}{\partial z} = \frac{1}{\text{Pe}} \left(\frac{\partial^2}{\partial z^2} - \alpha_{l,m}^2 \right) \bar{c}_1, \quad (13b)$$

associated with the boundary conditions,

$$\bar{w}_1 \rightarrow 0 \quad \bar{c}_1 \rightarrow 0 \text{ as } z \rightarrow \pm\infty. \quad (14)$$

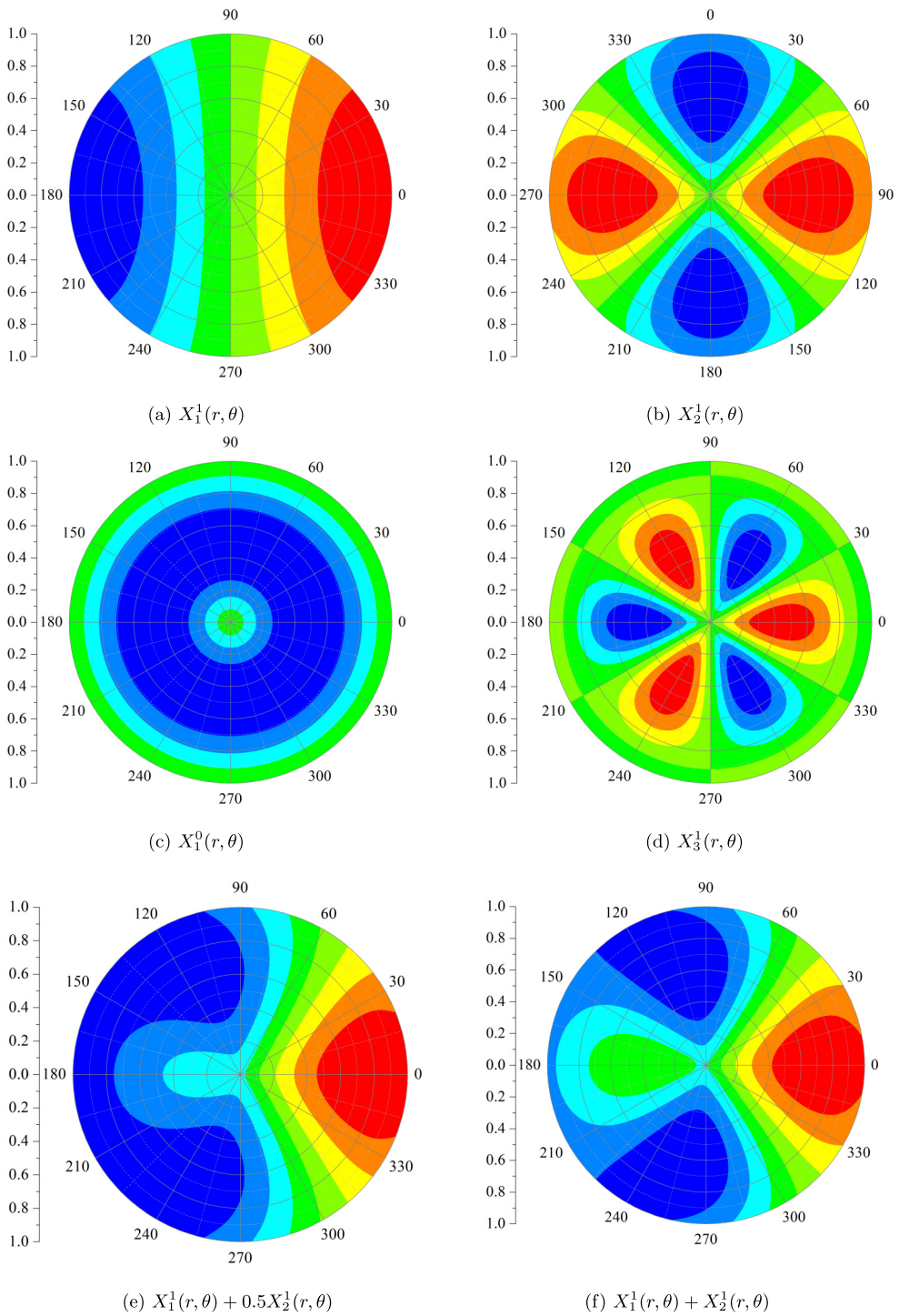


FIG. 2. First four single modes of the cylindrical harmonics, given in Eq. (10), and two mixed modes.

Our goal is to find the critical time τ_c for the given Pe and $R = (1/\bar{\mu})(\partial\bar{\mu}/\partial c_0)$, and the minimum Pe to mark the onset of fingering by solving Eqs. (13) and (14).

For the infinite layer, it is natural that $\bar{c}_1(\tau, x) = c_1^*(\tau, \zeta)$ and $\bar{w}_1(\tau, x) = w_1^*(\tau, \zeta)$, where $\zeta = \xi\sqrt{\text{Pe}}$ and ξ is the similarity variable introduced in Sec. II. Following a coordinate transformation to the similarity variable of ζ , stability equations can be expressed as

$$\left(\frac{\partial^2}{\partial\zeta^2} + \frac{1}{\bar{\mu}}\frac{\partial\bar{\mu}}{\partial\zeta}\frac{\partial}{\partial\zeta} - a^{*2}\right)w_1^* = -a^{*2}\frac{1}{\bar{\mu}}\frac{\partial\bar{\mu}}{\partial c_0}c_1^*, \quad (15a)$$

$$\tau\frac{\partial c_1^*}{\partial\tau} = \left(\frac{\partial^2}{\partial\zeta^2} + \frac{\zeta}{2}\frac{\partial}{\partial\zeta} - a^{*2}\right)c_1^* - \sqrt{\text{Pe}}\tau w_1^*\frac{dc_0}{d\zeta}, \quad (15b)$$

associated with the boundary conditions

$$w_1^* \rightarrow 0, \quad c_1^* \rightarrow 0 \quad \text{as} \quad \zeta \rightarrow \pm\infty. \quad (16)$$

Here, $a^* = \alpha_{l,m}\sqrt{\tau/\text{Pe}}$ and $\frac{dc_0}{d\zeta} = -\frac{1}{2\sqrt{\pi}}\exp(-\frac{\zeta^2}{4})$.

IV. SOLUTION PROCEDURE

A. Initial growth rate

The initial growth rate analysis is important in order to understand the dynamics of the disturbances at the early stages. For laterally unbounded systems, the initial growth rate (i.e., at $\tau = 0$) is calculated under QSSA [4,25], where Eq. (4a) is employed as the base concentration field. Here, we present an analytic approach without QSSA. At an initial state of $\tau \rightarrow 0$, since $a^* \rightarrow 0$ for finite $\alpha_{l,m}$, Eqs. (15) can be simplified as

$$\left(\frac{\partial^2}{\partial\zeta^2} + \frac{1}{\bar{\mu}}\frac{\partial\bar{\mu}}{\partial\zeta}\frac{\partial}{\partial\zeta}\right)w_1^* = 0, \quad (17a)$$

$$\tau\frac{\partial c_1^*}{\partial\tau} = \left(\frac{\partial^2}{\partial\zeta^2} + \frac{\zeta}{2}\frac{\partial}{\partial\zeta}\right)c_1^* - \sqrt{\text{Pe}}\tau w_1^*\frac{dc_0}{d\zeta}. \quad (17b)$$

In Eq. (17b), $\sqrt{\text{Pe}}\tau w_1^*\frac{dc_0}{d\zeta}$ is kept since $(\frac{\partial c_0}{\partial z})_{\tau=0} = -\delta(z)$ has a nonanalytic feature—here, $\delta(z)$ denote the Dirac delta function. Simple mathematical operations yield that the solution of the velocity disturbance can be expressed as

$$w_1^* = d_1 \int_{-\infty}^{\zeta} f(\chi)d\chi + d_2, \quad (18)$$

where

$$f(\chi) = \exp\left(-\int_{-\infty}^{\chi} \frac{1}{\bar{\mu}}\frac{d\bar{\mu}}{d\eta}d\eta\right) = \exp\left(-\int_1^{\bar{\mu}} \frac{1}{\bar{\mu}}d\bar{\mu}\right) = \frac{1}{\bar{\mu}(\chi)}. \quad (19)$$

The constants d_1 and d_2 should be zero to meet the boundary conditions $w_1^*(\tau, \pm\infty) \rightarrow 0$. Therefore, $w_1^* \rightarrow 0$ as $\tau \rightarrow 0$. This means that initially, there is no velocity disturbance and the instability motion is driven by the concentration disturbances.

Then, the concentration disturbances are governed by the following linear, homogeneous partial differential equation:

$$\tau\frac{\partial c_1^*}{\partial\tau} = \left(\frac{\partial^2}{\partial\zeta^2} + \frac{\zeta}{2}\frac{\partial}{\partial\zeta}\right)c_1^*. \quad (20)$$

Solving this equation using the variable separation technique and applying the superposition principle, we obtain

$$c_1^* = \sum_{n=0}^{\infty} A_n(\tau) \phi_n(\zeta) \quad (21)$$

for

$$\phi_n(\zeta) = (n! 2^{n+1} \sqrt{\pi})^{-1/2} H_n\left(\frac{\zeta}{2}\right) \exp\left(-\frac{\zeta^2}{4}\right), \quad (22)$$

where H_n represents the n th Hermite polynomials, and $\{\phi_n\}_{n=1}^{\infty}$ are orthonormal functions with respect to the weight $\exp(\zeta^2/4)$, i.e.,

$$\int_{-\infty}^{\infty} \phi_m(\zeta) \phi_n(\zeta) \exp\left(\frac{\zeta^2}{4}\right) d\zeta = \delta_{mn}. \quad (23)$$

The coefficients $A_n(\tau)$ can be obtained solving the following ordinary differential equation:

$$\tau \frac{dA_n}{d\tau} = -\lambda_n A_n \quad \text{for } n = 0, 1, 2, \dots, \quad (24)$$

which yields $A_n(\tau) = a_n \tau^{-\lambda_n}$, where a_n 's are arbitrary constants and $\lambda_n = (n+1)/2$ denotes the growth rate of the n th mode, $A_n(\tau) \phi_n(\zeta)$, defined as

$$\frac{1}{A_n} \frac{dA_n}{d\tau} = -\frac{\lambda_n}{\tau} \text{ as } \tau \rightarrow 0 \quad \text{for } n = 0, 1, 2, \dots \quad (25)$$

Clearly, the largest growth rate is associated with the first mode ($n = 0$), $a_0 \tau^{-1/2} \exp(-\zeta^2/4)$. Since the growth rate of the most dangerous mode

$$\frac{1}{A_0} \frac{dA_0}{d\tau} = -\frac{\lambda_0}{\tau} = -\frac{1}{2\tau} \text{ as } \tau \rightarrow 0 \quad (26)$$

is negative, the system is initially unconditionally stable.

B. Eigenanalysis

We use the following viscosity-concentration relation [4]:

$$\bar{\mu} = e^{R(1-c)}, \quad (27)$$

where

$$R = \ln \frac{\mu_+}{\mu_-} \quad (28)$$

is the log-viscosity (or log-mobility) ratio, and μ_+ and μ_- denote the viscosity of the displaced and displacing fluids, respectively. For the limiting case of $R \ll 1$, the stability equations can be rewritten as

$$\tau \frac{\partial c_1^*}{\partial \tau} = \left(\frac{\partial^2}{\partial \zeta^2} + \frac{\zeta}{2} \frac{\partial}{\partial \zeta} - a^{*2} \right) c_1^* - R^* \tilde{w}_1^* \frac{\partial c_0}{\partial \zeta}, \quad (29a)$$

$$\left(\frac{\partial^2}{\partial \zeta^2} - a^{*2} \right) \tilde{w}_1^* = -a^{*2} c_1^*, \quad (29b)$$

where $R^* = R\sqrt{\text{Pe}\tau}$, $\tilde{w}_1^* = w_1^*/R$, and $\frac{dc_0}{d\zeta} = -\frac{1}{2\sqrt{\pi}}\exp(-\frac{\zeta^2}{4})$. Using Sturm-Liouville theory [19,29], c_1^* , and \tilde{w}_1^* can be expressed as

$$c_1^* = \sum_{n=0}^{\infty} B_n(\tau)\phi_n(\zeta), \quad (30a)$$

$$\tilde{w}_1^* = \sum_{n=0}^{\infty} B_n(\tau)\psi_n(a^*, \zeta), \quad (30b)$$

where $\phi_n(\zeta)$ are given in Eq. (22), and $\psi_n(a^*, \zeta)$ satisfies

$$\left(\frac{\partial^2}{\partial\zeta^2} - a^{*2}\right)\psi_n = -a^{*2}\phi_n. \quad (31)$$

The solution to Eq. (31) corresponding to the boundary conditions, $\psi_n(a^*, \pm\infty) \rightarrow 0$, can be expressed as

$$\psi_n(a^*, \zeta) = \frac{a^*}{2} \left[\exp(a^*\zeta) \int_{\zeta}^{\infty} \exp(-a^*\chi)\phi_n(\chi)d\chi + \exp(-a^*\zeta) \int_{-\infty}^{\zeta} \exp(a^*\chi)\phi_n(\chi)d\chi \right]. \quad (32)$$

Using Eqs. (30) in Eq. (29a) and utilizing the orthogonality property of ϕ_n (i.e., by integrating with respect to ζ from $-\infty$ to ∞), we obtain

$$\tau \frac{dB_n}{d\tau} = -(\lambda_n + a^{*2})B_n + R^* \sum_{k=0}^{\infty} B_k \int_{-\infty}^{\infty} \phi_n(\zeta)\psi_k(a^*, \zeta)d\zeta. \quad (33)$$

Equation (33) can be written in the following matrix differential equation form:

$$\tau \frac{d\mathbf{B}}{d\tau} = \mathbf{E}\mathbf{B}, \quad (34a)$$

$$\mathbf{B} = [B_0, B_1, B_2, \dots], \quad (34b)$$

$$E_{mn} = -(\lambda_{m-1} + a^{*2})\delta_{mn} - \frac{1}{2\sqrt{\pi}}R^* \int_{-\infty}^{\infty} \phi_n\psi_m d\zeta, \quad (34c)$$

where the matrix \mathbf{E} is symmetric since $\int_{-\infty}^{\infty} \phi_j\psi_i d\zeta = \int_{-\infty}^{\infty} \phi_i\psi_j d\zeta$. System (34) is nonautonomous since a^* and R^* are time dependent, and hence \mathbf{E} is time dependent. The growth rate of the perturbations is defined as

$$\sigma_{\tau}^* = \frac{1}{2} \frac{1}{\mathbf{B}^{\top}\mathbf{B}} \left(\frac{d\mathbf{B}^{\top}}{d\tau}\mathbf{B} + \mathbf{B}^{\top}\frac{d\mathbf{B}}{d\tau} \right). \quad (35)$$

Using Eq. (34a) and through basic matrix operations, Eq. (35) can be rewritten as

$$\sigma_{\tau}^* \tau = \frac{1}{\mathbf{B}^{\top}\mathbf{B}} \mathbf{B}^{\top} \left(\frac{\mathbf{E}^{\top} + \mathbf{E}}{2} \right) \mathbf{B}. \quad (36)$$

For a symmetric matrix \mathbf{E} , i.e., $\mathbf{E}^{\top} = \mathbf{E}$, Eq. (36) further reduces to

$$\sigma_{\tau}^* \tau = \frac{1}{\mathbf{B}^{\top}\mathbf{B}} \mathbf{B}^{\top} \mathbf{E} \mathbf{B}. \quad (37)$$

It is to recall that symmetric matrices are normal and the eigenvalues of normal matrices are real. Through eigenanalysis, it can be shown that

$$\sigma_{\tau}^* \tau = \max\{\text{eig}(\mathbf{E})\}, \quad (38)$$

where $\max\{\text{eig}(\mathbf{E})\}$ corresponds to the maximum eigenvalue of \mathbf{E} . For the limiting case of $\tau \rightarrow 0$, \mathbf{E} becomes a diagonal matrix and the entries are given by $E_{ij} = (-i/2)\delta_{ij}$. The eigenvalues of \mathbf{E} are the diagonal entries of this matrix. Therefore, the largest eigenvalue is $-1/2$, i.e., $\sigma_\tau^* \tau = -1/2$, and the corresponding eigenvector is $[1, 0, 0, \dots]^\top$. This reconfirms our initial growth rate results discussed in Sec. IV A.

C. Quasi-steady-state approximation

The eigenanalysis presented in Sec. IV B is valid only in the limiting case of $R \ll 1$. Therefore, we seek an alternative approach applicable for all admissible values of R . We use QSSA [4], which is widely used in the stability analysis of time-dependent base flow. Employing QSSA, the spatial and temporal dependencies of the perturbations are expressed in terms of the normal modes [20,21],

$$c_1^*(\tau, \zeta) = \mathcal{A}(\tau)\Phi(\zeta), \quad w_1^*(\tau, \zeta) = \mathcal{A}(\tau)\Psi(a^*, \zeta), \quad (39)$$

where \mathcal{A} is the amplitude of the perturbations and the growth rate is defined as

$$\sigma_\tau^* = \frac{1}{\mathcal{A}} \frac{d\mathcal{A}}{d\tau}. \quad (40)$$

To avoid the notational complexity, we have used σ_τ^* to denote the growth rate obtained from both eigenanalysis and QSSA. However, in the analysis and discussion of the results (Secs. VI and VII), we will explicitly mention the method used to calculate the growth rate.

Using Eqs. (39) and (40) in (15) and (16), we obtain

$$\left(\frac{\partial^2}{\partial \zeta^2} + \frac{\zeta}{2} \frac{\partial}{\partial \zeta} - a^{*2} - \sigma_\tau^* \tau \right) \Phi = -\text{Pe} \sqrt{\tau} \frac{1}{2\sqrt{\pi}} \exp\left(-\frac{\zeta^2}{4}\right) \Psi, \quad (41a)$$

$$\left(\frac{\partial^2}{\partial \zeta^2} + \frac{1}{\bar{\mu}} \frac{\partial \bar{\mu}}{\partial \zeta} \frac{\partial}{\partial \zeta} - a^{*2} \right) \Psi = -a^{*2} \frac{1}{\bar{\mu}} \frac{\partial \bar{\mu}}{\partial c_0} \Phi, \quad (41b)$$

and

$$\Phi \rightarrow 0 \quad \text{and} \quad \Psi \rightarrow 0 \quad \text{as} \quad \zeta \rightarrow \pm\infty. \quad (42)$$

Using the viscosity-concentration relation (27), Eq. (41b) can be further simplified to

$$\left[\frac{\partial^2}{\partial \zeta^2} + R \frac{1}{2\sqrt{\pi}} \exp\left(-\frac{\zeta^2}{4}\right) \frac{\partial}{\partial \zeta} - a^{*2} \right] \Psi = a^{*2} R \Phi. \quad (43)$$

We solve Eqs. (41a) and (43) subjected to the boundary conditions (42) for $\tau > 0$.

For the limiting case of $R \ll 1$, the growth rate calculated from the eigenanalysis is compared with that obtained from QSSA in Fig. 3, in which the order of the approximation is the number of terms used in the expression for c_1^* and w_1^* in Eqs. (30). As shown in this figure, the present analytical and numerical solutions show good agreement.

V. NONLINEAR NUMERICAL SIMULATIONS

We solved the nonlinear governing Eqs. (2) and (27) numerically by using the finite-element method (FEM)-based commercial code COMSOL MULTIPHYSICS. The velocity field is modeled using Darcy's law (dl) for fluid flow in Darcian porous media. In addition, the solute transport equation is modeled using the diluted species in porous media (tds) of COMSOL MULTIPHYSICS. Because these velocity and concentration fields are tied up by Eq. (27), we should solve Eqs. (2) iteratively. The above equations correspond to $\varepsilon = 1$, $D = 1/\text{Pe}$, $\rho = 1$, and $K = 1$ in the COMSOL MULTIPHYSICS. In the present study, we chose the calculation domain as $x^2 + y^2 \leq 1$ and $-L \leq z \leq L$, and imposed the no-flux boundary conditions at $x^2 + y^2 = 1$, $c = 1$ and $w = 1$ at $z = -L$, and $c = 0$ and $p = 0$

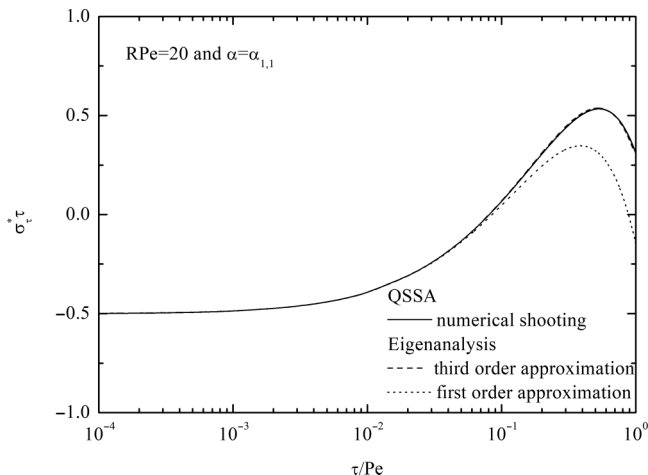


FIG. 3. Comparison of the growth rates obtained from the various methods for the case of $RPe = 20$ and $a_{l,m} = a_{1,1}$.

at $z = L$, respectively. We used the following initial condition:

$$c = 1 - G(z) \text{ and } p = 0 \text{ at } \tau = 0, \quad (44)$$

where $G(z)$ is the smoothed Heaviside step function. We solved the time-dependent problem using the implicit backward differentiation formula (BDF) scheme with relative error of 10^{-4} .

For the example case of $Pe = 50$, the concentration fields for the stable ($R = -1$), neutral ($R = 0$), and unstable ($R = 1$) cases are compared in Fig. 4. As shown in this figure, we cannot observe fingering instabilities for the stable and neutral cases. Comparing Figs. 2 and 4(c), it is evident that several modes that interact at the initial time ($\tau = 0$) lead to the dominance of the $X_1^1(r, \theta)$ and $X_2^1(r, \theta)$ modes at $\tau \approx 20$, and that if $X_1^1(r, \theta)$ at $\tau > 30$.

VI. RESULTS AND DISCUSSIONS

For laterally unbounded systems, the initial growth rate is positive for a certain range of wave number [4,25]. The present initial growth rate analysis shows that the system is unconditionally stable with respect to any disturbance. Thus, the present study explains the stable displacement of low viscosity samples observed near the injection region in a low-flow rate run [3,22,23].

Figure 5(a) shows the neutral stability curves—the region above these curves denotes the unstable state, i.e., $\sigma_\tau^* > 0$, whereas the region below these curves corresponds to the region of stability. As shown in these figures, for the limiting case of $R \ll 1$, the eigenanalysis and QSSA solutions produce almost identical stability conditions. The stability curve redrawn in the $RPe\tau^{1/2} - \alpha_{l,m}/RPe$ plane exhibits a possibility for the restabilization of temporarily unstable modes [see Fig. 5(b)]. This curve shows that for a given RPe , all disturbances decay when $RPe\sqrt{\tau} < 5.646$; however, as time increases, some disturbances will grow only if $\alpha_{l,m}/RPe < 0.1172$. We define the critical time τ_c as the time at which a disturbance starts growing. This phenomenon is also observed in buoyancy-driven fingering instability [30].

Unlike the horizontally unbounded domain, the presence of cylinder boundaries imposes a restriction on the feasible wave number given by Eq. (11) and these take discrete values. For the nine smallest wave numbers, the rescaled critical times are plotted as a function of RPe in Fig. 6. It is observed that the nonaxisymmetric mode of $J_1(\alpha_{1,1}r)\exp(i\theta)$ is the most unstable mode, which yields the minimum RPe to induce the convective motion. We obtain the critical values of $(RPe)_c$

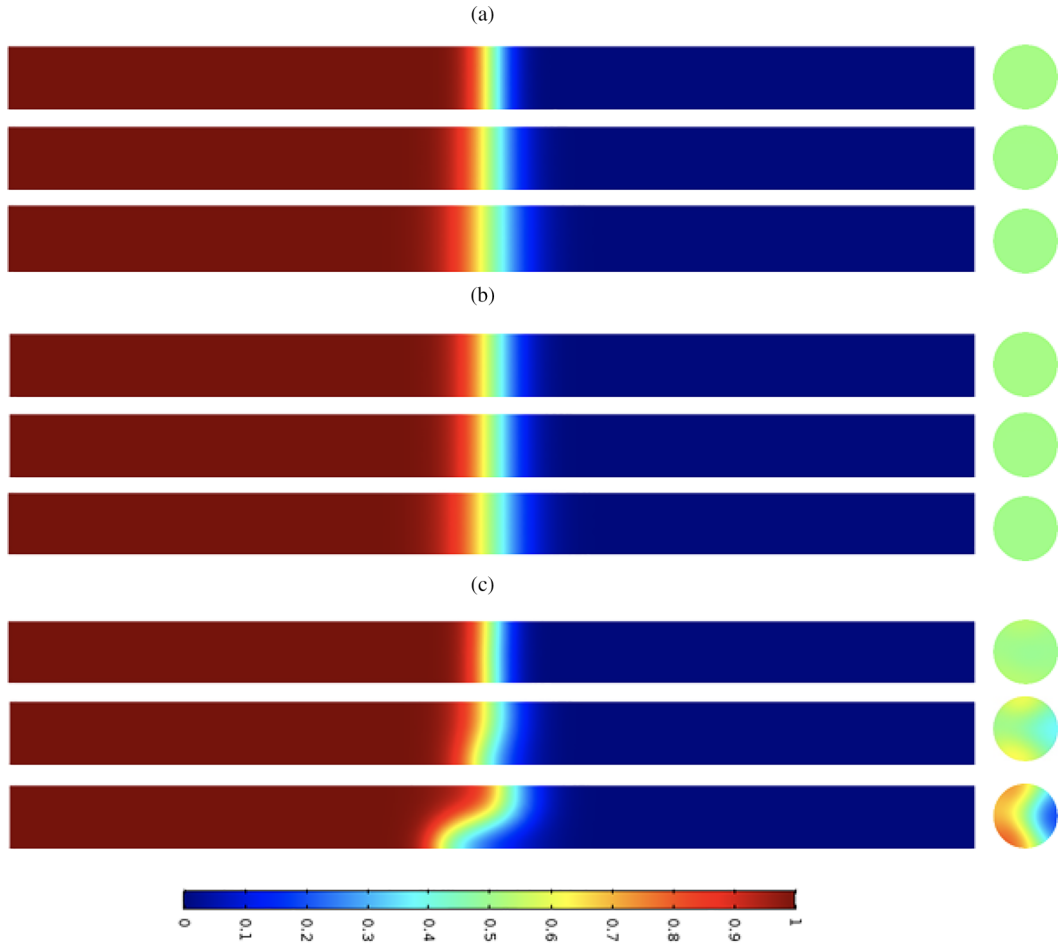


FIG. 4. Temporal evolution of the $x - z$ sliced at $y = 0$ (left) and $x - y$ sliced at $z = 0$ (right) concentration fields for $Pe = 50$: (a) stable ($R = -1$), (b) neutral ($R = 0$), and (c) unstable ($R = 1$) systems. From top to bottom: $\tau = 10, 20$, and 30 .

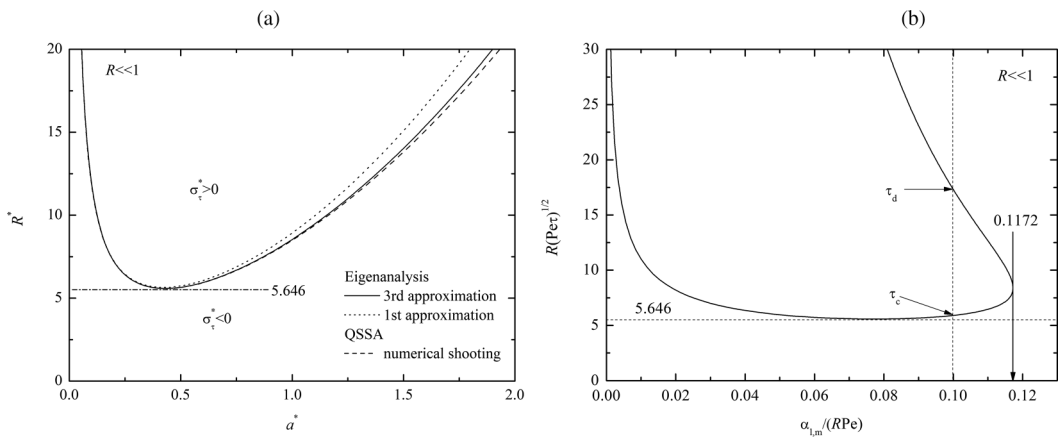


FIG. 5. Comparison of neutral stability curves from the various methods: (a) $R^* - a^*$ plane and (b) $RPe\tau^{1/2} - \alpha_{1,m}/(RPe)$ plane.

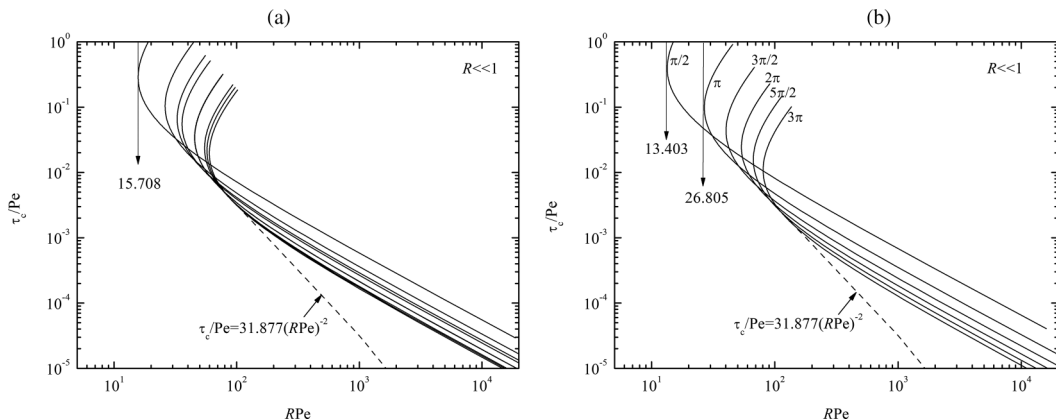


FIG. 6. Critical-time curves for (a) cylindrical three-dimensional case and (b) two-dimensional one. In (a), the lowest nine modes, which are summarized in Table I, are given from left to right. It is observed that the $\alpha_{4,1}$ and $\alpha_{1,2}$ modes are almost indistinguishable.

for the most dangerous disturbance as

$$(RPe)_c = \frac{\alpha_{1,1}}{0.1172} = 15.708 \quad \text{for } R \ll 1. \quad (45)$$

Recently, Nijjer *et al.* [21] reported a similar observation for two-dimensional infinite stripes with lateral periodicity, for which the allowable dimensionless wave numbers are $\alpha = n\pi$, $n = 1, 2, 3, \dots$. Considering the periodic lateral boundary conditions, Eq. (45) reduces to

$$(RPe)_c = \frac{\pi}{0.1172} = 26.805 \quad \text{for } R \ll 1, \quad (46)$$

which explains Fig. 6(d) by Nijjer *et al.* [21] quite well. If the stability curve is redrawn in the $RPe \tau^{1/2} - \alpha_{l,m}/RPe$ domain, a possibility for restabilization of the temporarily unstable modes appears, as shown in Fig. 5(b). The occurrence of restabilization of the transient unstable modes is also observed in the studies of Nijjer *et al.* [21] [see their Fig. 5(c)]. Extending our analysis to the system investigated by Pramanik and Mishra [20], for which the allowed dimensionless wave numbers are $\alpha = n\pi/2$, where $n = 1, 2, 3, \dots$, Eq. (45) becomes

$$(RPe)_c = \frac{\pi/2}{0.1172} = 13.403 \quad \text{for } R \ll 1. \quad (47)$$

Here, it should be kept in mind that the Péclet number defined in this paper is half of those defined in [20,21] because in those studies the Péclet number is based on the full width [20,21] of the stripe, rather than the radius of the cylinder.

For the case of high Péclet number (e.g., $RPe > 50$), the radial boundary effects are unimportant and $D/(RW_0)^2$ or D/W_0^2 seems to be the proper timescale. The critical time decreases with increasing RPe and, if all the possible wave numbers are superimposed, the following asymptotic relation

TABLE I. A few smallest zeros of $\alpha_{l,m}$ given in Eq. (9). These correspond to the least stable modes.

(l, m)	(1,1)	(2, 1)	(0, 1)	(3, 1)	(4, 1)	(1, 2)	(5, 1)	(2, 2)	(0, 2)
$\alpha_{l,m}$	1.841	3.054	3.832	4.201	5.318	5.331	6.416	6.706	7.016

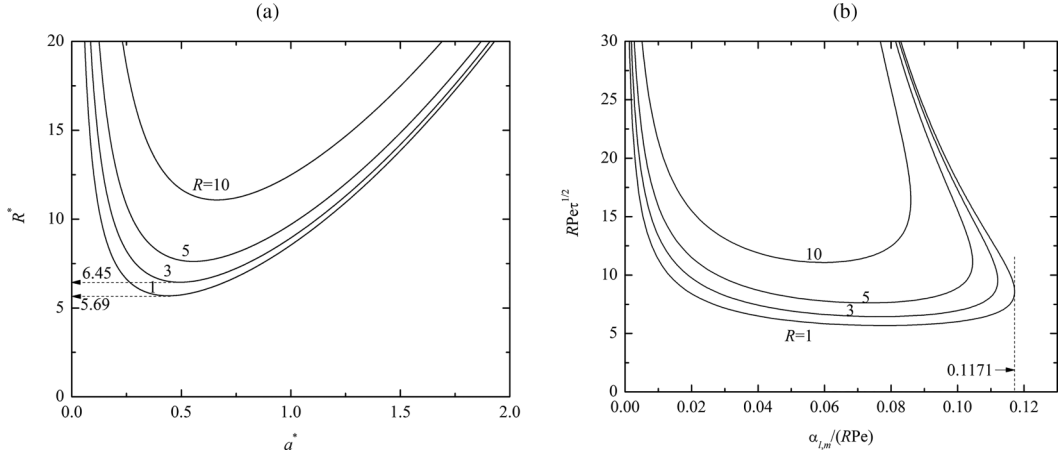


FIG. 7. Neutral stability curves obtained from the QSSA for the several finite values of R : (a) $R^* - \alpha^*$ plane and (b) $RPe\tau^{1/2} - \alpha_{l,m}/(RPe)$ plane.

results,

$$t_c = 31.877D/(RW_0)^2 \quad \text{for } R \ll 1 \text{ and } RPe > 50, \quad (48)$$

which can be drawn from Fig. 5(b), i.e., $R_c^* [= R(\tau_c Pe)^{1/2}] = 5.646$. For the rectilinear system, where the lateral boundary effects are unimportant, D/W_0^2 has been used for the timescale and Eq. (47) can be applied. In addition, Eq. (48) can be applied to the infinite strip systems [20,21] for the case of $RPe > 50$, where the lateral boundary effects play little roles on the critical time.

The eigenanalysis is not applicable for all values of τ , R , and Pe . Therefore, the QSSA discussed in Sec. IV C is employed in general. For several value of R , neutral stability curves obtained from QSSA are compared in Fig. 7. Based on these neutral curves, the critical times for the finite- R cases are summarized in Fig. 8. As shown in Figs. 6 and 8, there exists a critical Péclet number and the corresponding critical wave number. It is observed that the nonaxisymmetric mode, $J_1(\alpha_{1,1}r) \exp(i\theta)$, is the most unstable mode near the critical Péclet number.

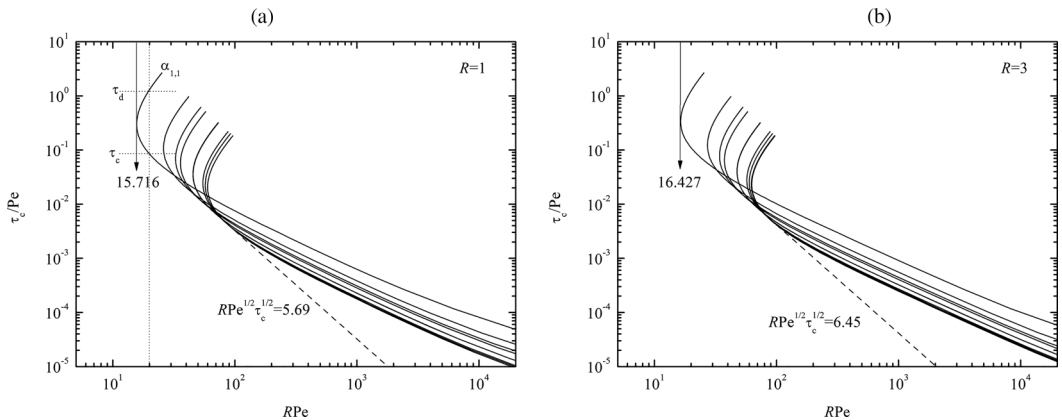


FIG. 8. Critical-time curves for the smallest nine wave numbers. The modes summarized in Table I are given from left to right and the (4,1) and (1,2) modes are indistinguishable in this figure. (a) $R = 1$ and (b) $R = 3$.

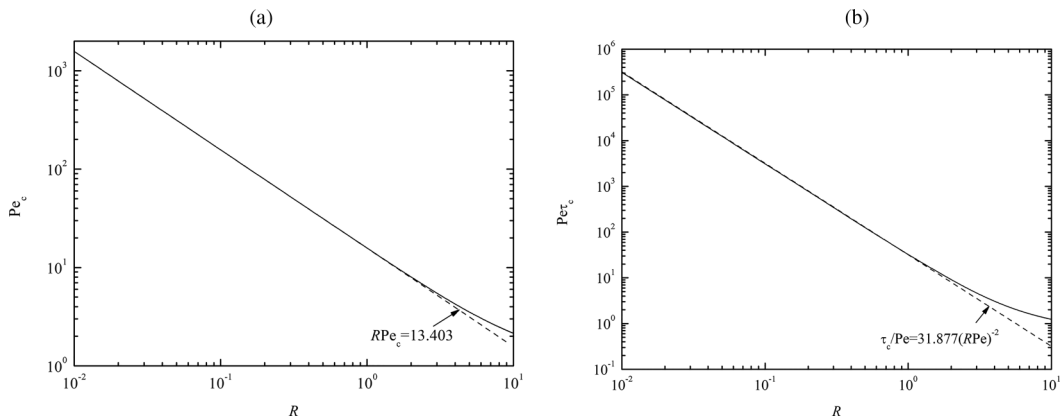


FIG. 9. Critical conditions for finite R : (a) critical Péclet number and (b) critical time for the high RPe case.

Another important finding of the present linear analysis is that there exists the onset time τ_c , from which the system becomes unstable, and the decay times τ_d , from which the stability can be restored. Nijjer *et al.* [21] also discussed this restabilization in the linearly unstable regime. Based on these findings, the critical Péclet number and the critical time for the high- RPe case are summarized in Fig. 9. From these figures, it can be known that the larger R is, the more important the viscous fingering effect. For the case of moderate viscosity contrast, $R \leq 1$, Eqs. (45) and (48) give a good approximation for the critical conditions.

Using nonlinear numerical simulations of viscous fingering in a miscible slice, De Wit *et al.* [16] reported $t^*(= \tau_c Pe) \propto R^{-2}$, which is in accordance with Eq. (48). Note that for very small values of R , the onset time and the critical Péclet number become very large. This explains the absence of fingering instability to low viscosity samples [Fig. 9(a)] in small chromatographic columns, for which $\tau < \tau_c$, and for small displacing speed [Fig. 9(b)], for which $Pe < Pe_c$.

To understand the effects of the lateral boundaries on the nonlinear fingering instability in the cylindrical system, we perform nonlinear numerical simulations using COMSOL MULTIPHYSICS in the present study. Figure 10 compared the temporal evolution of the concentration field for $Pe = 15$ and 25. When $Pe = 15$, no visual difference between neutral ($R = 0$) and the unfavorable ($R = 1$) viscosity contrasts was identified [compare Figs. 10(a) and 10(b)]. However, for $Pe = 25$, significant differences were observed between the neutral and the unfavorable viscosity contrasts [compare Figs. 10(c) and 10(d)]. From the above findings, we estimated $15 < Pe_c < 25$ for $R = 1$ —in accordance with the theoretical prediction based on the linear stability analysis, i.e.,

$$Pe_c = \frac{\alpha_{1,1}}{0.1171} = 15.716. \quad (49)$$

In addition, for $R = 1$ and $Pe = 25$, the restabilization phenomenon is found and the most unstable mode is the $X_1^1(r, \theta)$ mode [see Fig. 2(a)], as predicted through linear stability analysis [see Fig. 8(a)]. The linear stability analysis yields that the system corresponding to $R = 1$ and $Pe = 25$ is temporally unstable, as shown in Fig. 8(a). The corresponding numerical simulations are summarized in Fig. 10(d). During the initial period, the instability motion is developed as time goes on. At a later time, the instability level reaches its maximum value and decays owing to the stabilization induced by diffusion. For time larger than $\tau \geq 80$, we clearly observed that the stabilization effect of diffusion weakens the concentration nonuniformity caused by instability motion. This indicates that the present linear stability analysis and numerical simulation are in good agreement.

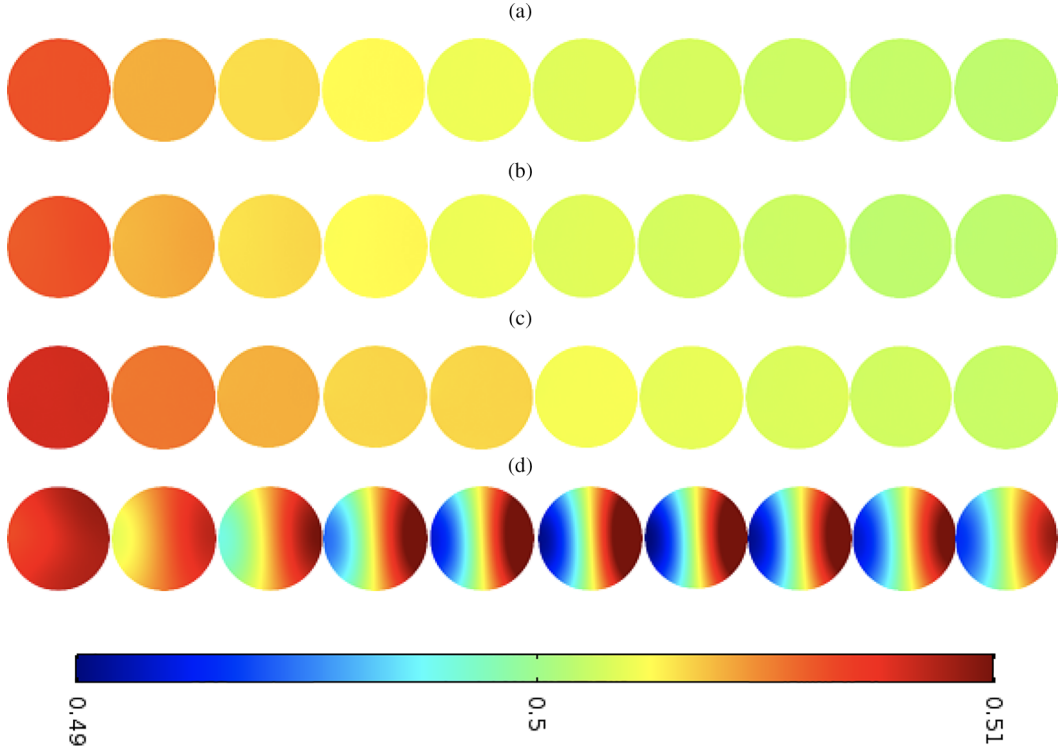


FIG. 10. Temporal evolution of $x - y$ sliced concentration fields for (a) $R = 0$ and $Pe = 15$, (b) $R = 1$ and $Pe = 15$, (c) $R = 0$ and $Pe = 25$, and (d) $R = 1$ and $Pe = 25$. From left to right, $\tau = 10, 20, 30, 40, 50, 60, 70, 80, 90$, and 100 . Concentration fields are taken at $z = 0$.

Linear stability analysis approximates the critical Péclet numbers as

$$Pe_c = \frac{\pi}{0.1171} = 26.828 \quad \text{for } R = 1 \text{ and periodic system,} \quad (50)$$

and

$$Pe_c = \frac{\pi/2}{0.1171} = 13.414 \quad \text{for } R = 1 \text{ and symmetric or no-flux system.} \quad (51)$$

Figure 11 shows the concentration fields for $R = 1$ and periodic as well as symmetric (or no-flux) boundary conditions for different values of Pe such that $Pe \gtrsim Pe_c$. Equations (46)–(48) reveal that the present three-dimensional cylindrical system is more unstable than the two-dimensional periodic one [21]. The same conclusion can be drawn from Figs. 10 and 11, which show that the cylindrical system with $R = 1$ and $Pe = 25$ is unstable [see Fig. 10(d)], whereas the two-dimensional periodic system with $R = 1$ and $Pe = 35$ is stable [see Fig. 11(c)]. Furthermore, from Eqs. (47) and (48), and Fig. 11, it can be concluded that in a two-dimensional domain, the no-flux condition is more unstable than the periodic one. For $R = 1$ and $Pe = 300$, the concentration fields in two- and three-dimensional systems are shown in Fig. 12 for the no-flux boundary conditions. This figure clearly shows that the fingering dynamics in two-dimensional systems is significantly different from that in three-dimensional systems. Since the lateral boundaries do not play a significant role on the onset and the growth of fingers for large Pe and small τ , we restrict our discussion in three-dimensional (3D) cylindrical geometries for (a) small and intermediate Pe and (b) intermediate and large τ .

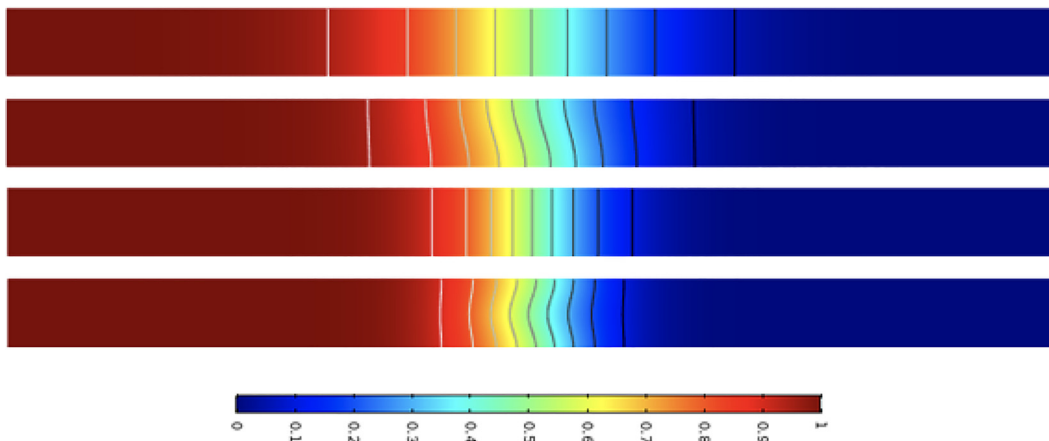


FIG. 11. Effect of the boundary conditions on the onset of VF for $R = 1$. Top to bottom: $Pe = 15, 25, 35,$ and 50 . The two top panels are for the no-flux condition, while the bottom two panels are for the periodic condition.

Figure 13 shows the temporal evolution of the concentration field for $R = 1$ and $Pe = 50, 100,$ and 200 . This figure clearly shows that the concentration fields are strongly dependent on Pe . With an increasing Pe , the number of initial fingers and the length of the fingers increase.

The effect of R on the concentration fields for the case of $RPe = 300$ and $\tau/Pe = 0.1$ such that $R^2Pe\tau = 9 \times 10^3$, and $RPe = 200$ and $\tau/Pe = 0.25$ such that $R^2Pe\tau = 10^4$, are summarized in Figs. 14 and 15, respectively. From the present linear stability analysis summarized in Fig. 9, the stability characteristics are governed by $R^2Pe\tau$ if $RPe > 50$ and $R \leq 2$. Numerical simulations for $RPe = 300$ and 200 are summarized in Figs. 13 and 14. The simulation results for $RPe = 200$ and $R \leq 2$ given in Fig. 14 show the instability motions nearly independent of the value of R , which is in good agreement with the linear analysis. However, as shown in Fig. 13, for the case of $RPe = 300$, the value of R plays roles in the instability patterns if $R > 2$. Furthermore, it seems that the strength of instability grows with $R^2Pe\tau$.

Suekane *et al.* [24] studied experimentally fingering instability in three-dimensional cylindrical geometry. We perform nonlinear simulations corresponding to their experimental conditions and the

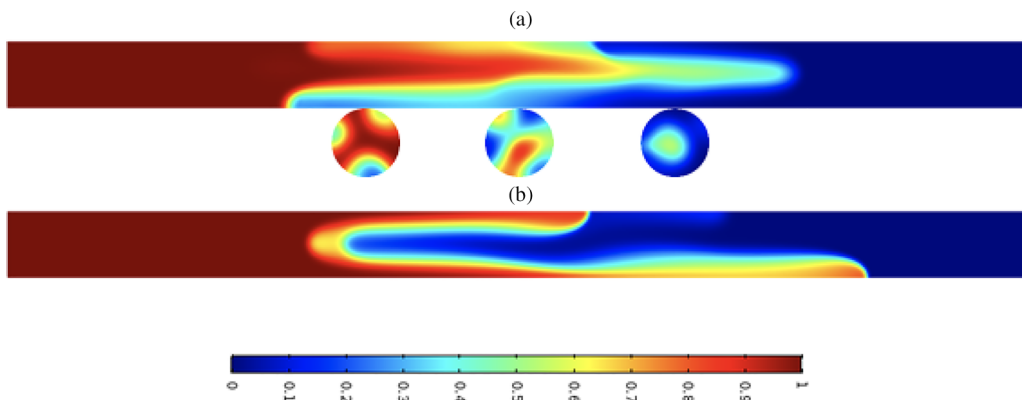


FIG. 12. Concentration fields for $R = 1$, $Pe = 300$ and $\tau = 50$. (a) Three-dimension and no-flux condition—concentration field is taken at $y = 0$ (upper panel) and $z = -5, 0,$ and 5 (lower panel). Calculation domain is $0 \leq r \leq 1$ and $-15 \leq z \leq 15$. (b) Two-dimension and no-flux condition.

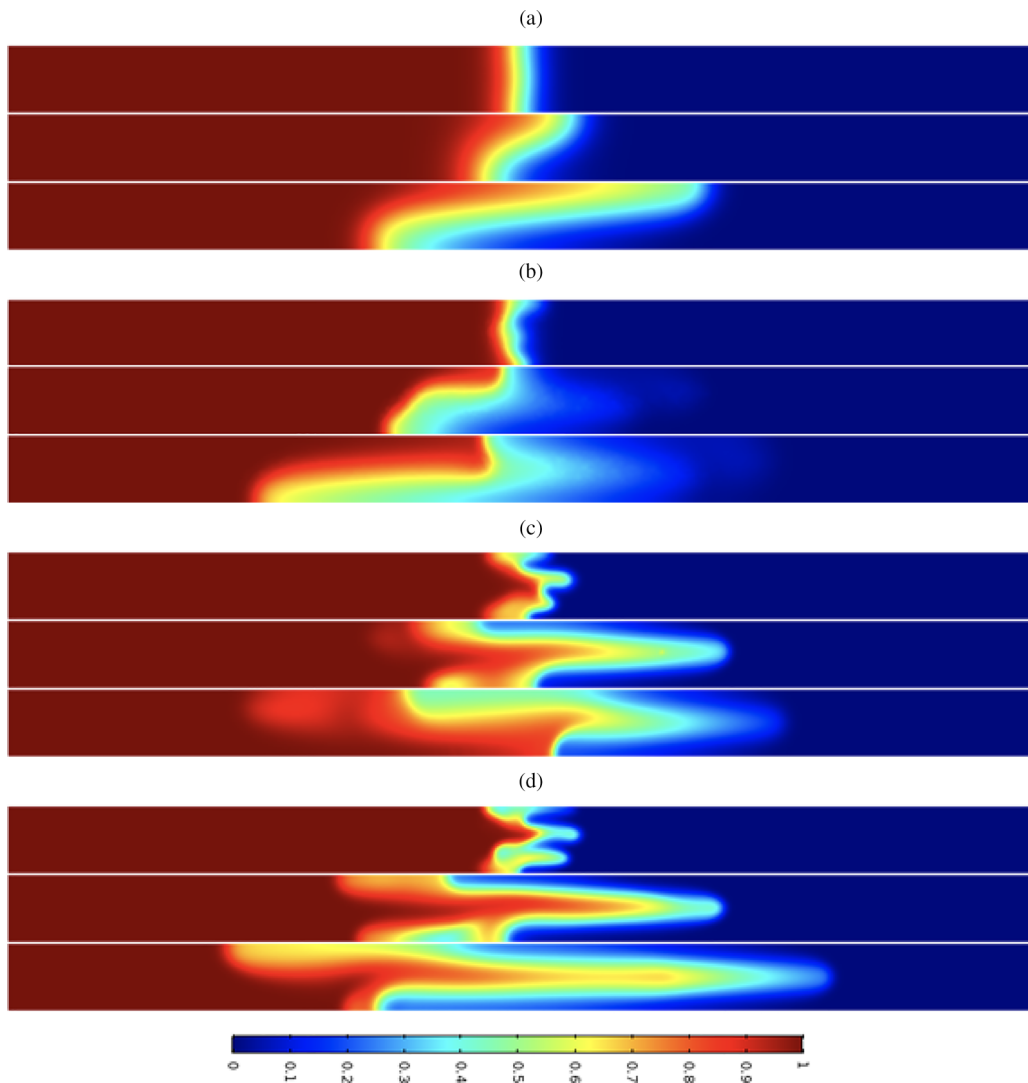


FIG. 13. Effect of Pe on the growth of VF for $R = 1$: (a) $Pe = 50$, (b) $Pe = 100$, (c) $Pe = 150$, and (d) $Pe = 200$. From top to bottom: $\tau = 10, 30$, and 50 . Concentration field is taken at $y = 0$ (upper panel) and $z = -5, 0$, and 5 (lower panel). Calculation domain is $0 \leq r \leq 1$ and $-15 \leq z \leq 15$.

corresponding physical properties: $\kappa = 1.3 \times 10^{-10} \text{ m}^2$, $b = 16 \text{ mm}$, and $D = 1.0 \times 10^{-10} \text{ m}^2 \text{ s}^{-1}$. Figure 16 shows temporal evolution of the fingering instability in three-dimensional cylindrical geometry for $R = \ln 10$ and $Pe = 1.3 \times 10^5$. Our simulation results corresponds to the L2-M2 fluid pair of Suekane *et al.* [24] and it is observed that the current numerical results are in accordance with the experimental study.

VII. CONCLUSION

The onset of miscible viscous fingering in a packed column has been analyzed theoretically and numerically. Using linear stability theory, we predicted that the onset time of fingering motion is a function of R and Pe ; the latter is defined based on the radius of a cylinder. The initial growth

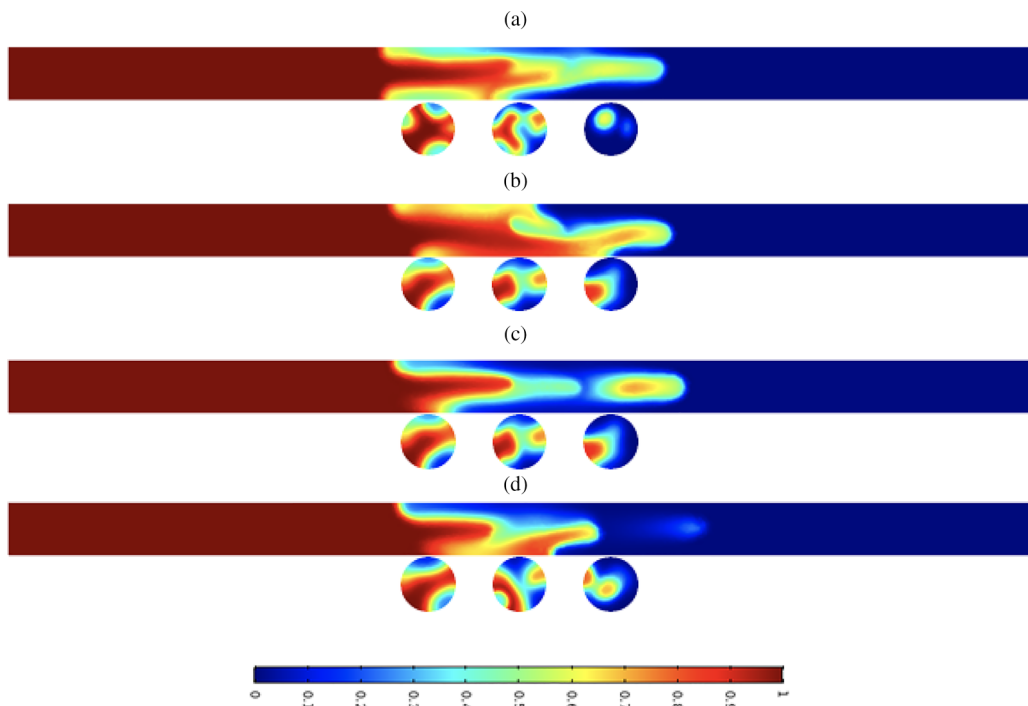


FIG. 14. Effect of R on the concentration fields for $R\text{Pe} = 300$ and $\tau/\text{Pe} = 0.1$, i.e., $R^2\text{Pe}\tau = 9 \times 10^3$. (a) $R = 1$, $\text{Pe} = 300$, and $\tau = 30$, (b) $R = 1.5$, $\text{Pe} = 200$, and $\tau = 20$, (c) $R = 2$, $\text{Pe} = 150$, and $\tau = 15$, and (d) $R = 3$, $\text{Pe} = 100$, and $\tau = 10$. Concentration fields are taken at $y = 0$ (upper panel) and $z = -2.5, 0$, and 2.5 (lower panel). Calculation domain is $0 \leq r \leq 1$ and $-20 \leq z \leq 20$.

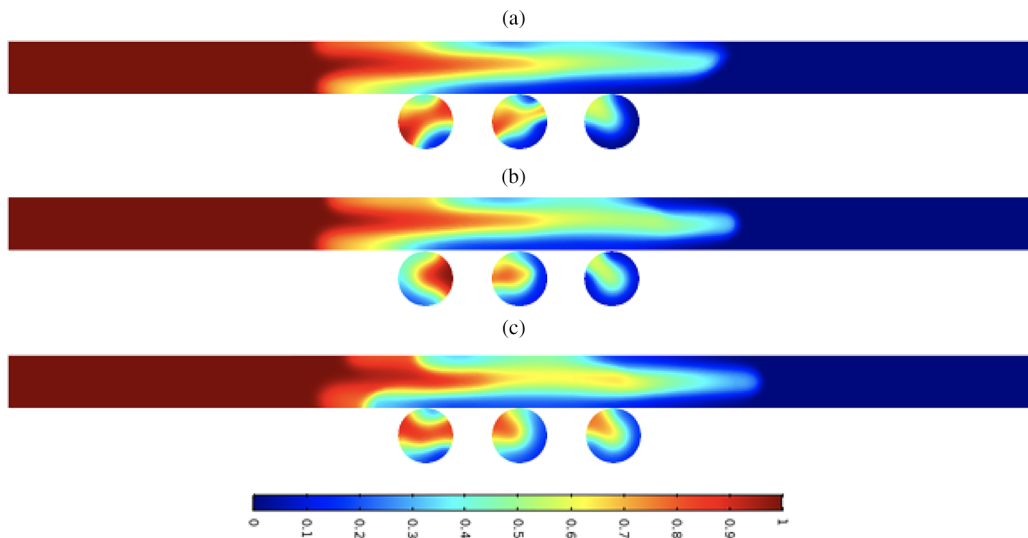


FIG. 15. Effect of R on the concentration fields for $R\text{Pe} = 200$ and $\tau/\text{Pe} = 0.25$, i.e., $R^2\text{Pe}\tau = \times 10^4$. (a) $R = 0.5$, $\text{Pe} = 400$, and $\tau = 100$, (b) $R = 1$, $\text{Pe} = 200$, and $\tau = 50$, (c) $R = 2$, $\text{Pe} = 100$, and $\tau = 25$. Concentration fields are taken at $y = 0$ (upper panel) and $z = -2.5, 0$, and 2.5 (lower panel). Calculation domain is $0 \leq r \leq 1$ and $-20 \leq z \leq 20$.

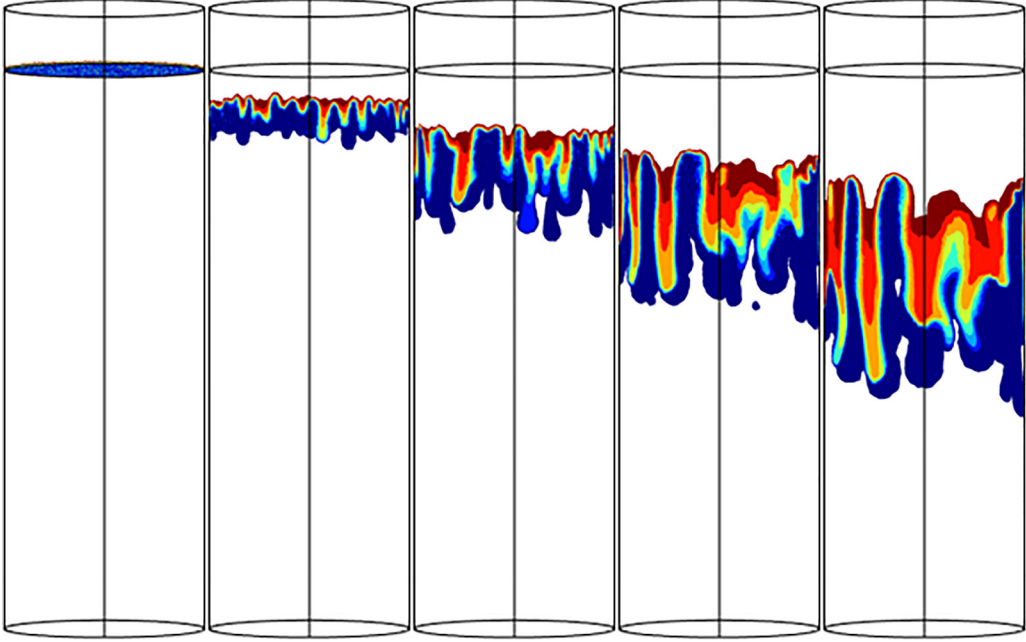


FIG. 16. Temporal evolution of the isoconcentration surface for $R = \ln 10$ and $Pe_S (= 2Pe) = 1.3 \times 10^5$. From left to right and top to bottom: $t = 0, 10, 20, 30, 40, 50, 60, 70, 80,$ and 90 from the left to the right. Here, Pe_S denotes the Péclet number defined in Suekane *et al.* [24]. The dimensionless time can be calculated as $\tau = PeDt/b^2$.

rate analysis shows that the system studied here is unconditionally stable. We determine the critical Péclet number and the critical time for the onset of fingering motion using a quasi-steady-state approximation.

In the nonlinear regime, numerical simulations in two-dimensional (2D) and the three-dimensional (3D) domains were performed and the critical parameters for the onset of instability were identified. In 2D, the onset and the growth of VF are strongly dependent on the lateral boundary conditions, and the critical Péclet number obtained from the present linear stability analysis and the nonlinear numerical simulation are in good qualitative agreement. Further, comparison between the present 2D and 3D simulations yields that 2D approximations fail to identify many important properties of VF in the cylindrical geometry due to its 3D nature. We successfully reproduced various growth mechanisms of VF that were reported in the experimental studies of VF.

Due to the computational complexities, we did not perform further numerical simulation for the high Pe and large τ to study the ultimate flow regimes as shown in the studies of Nijjer *et al.* [21]. However, we propose that similar investigation in the 3D cylindrical system should be of interest for future studies.

The data that support the findings of this study are available within the article.

ACKNOWLEDGMENTS

M.C.K. acknowledges the support of the Basic Science Research Program through the National Research Foundation of Korea (NRF) funded by the Ministry of Education (NRF-2021R1I1A3A04037444). S.P. is supported by Start-Up Research Grant (No. NSRG/2021/001269) by the Science and Engineering Research Board, Department of Science and Technology, Government of India.

- [1] G. M. Homsy, Viscous fingering in porous media, *Annu. Rev. Fluid Mech.* **19**, 271 (1987).
- [2] R. L. Slobod, R. A. Thomas *et al.*, Effect of transverse diffusion on fingering in miscible-phase displacement, *Soc. Pet. Eng. J.* **3**, 9 (1963).
- [3] T. K. Perkins, O. C. Johnston, R. N. Hoffman *et al.*, Mechanics of viscous fingering in miscible systems, *Soc. Pet. Eng. J.* **5**, 301 (1965).
- [4] C. T. Tan and G. M. Homsy, Stability of miscible displacements in porous media: Rectilinear flow, *Phys. Fluids* **29**, 3549 (1986).
- [5] D. Pritchard, The linear stability of double-diffusive miscible rectilinear displacements in a Hele-Shaw cell, *Eur. J. Mech. B Fluids* **28**, 564 (2009).
- [6] S. Pramanik, A. De Wit, and M. Mishra, Viscous fingering and deformation of a miscible circular blob in a rectilinear displacement in porous media, *J. Fluid Mech.* **782**, R2(2015).
- [7] R. Luo, Y. Chen, and S. Lee, Particle-induced viscous fingering: Review and outlook, *Phys. Rev. Fluids* **3**, 110502 (2018).
- [8] M. Hopp-Hirschler, M. S. Shadloo, and U. Nieken, Viscous fingering phenomena in the early stage of polymer membrane formation, *J. Fluid Mech.* **864**, 97 (2019).
- [9] R. Moosavi, A. Kumar, A. De Wit, and M. Schröter, Influence of mineralization and injection flow rate on flow patterns in three-dimensional porous media, *Phys. Chem. Chem. Phys.* **21**, 14605 (2019).
- [10] A. Kumar and M. Mishra, Boundary effects on the onset of miscible viscous fingering in a Hele-Shaw flow, *Phys. Rev. Fluids* **4**, 104004 (2019).
- [11] T. Gao, M. Mirzadeh, P. Bai, K. M. Conforti, and M. Z. Bazant, Active control of viscous fingering using electric fields, *Nat. Commun.* **10**, 1 (2019).
- [12] C. Rana, S. Pramanik, M. Martin, A. De Wit, and M. Mishra, Influence of Langmuir adsorption and viscous fingering on transport of finite size samples in porous media, *Phys. Rev. Fluids* **4**, 104001 (2019).
- [13] V. Sharma, H. B. Othman, Y. Nagatsu, and M. Mishra, Viscous fingering of miscible annular ring, *J. Fluid Mech.* **916**, A14(2021).
- [14] L. Vienne and S. Marié, Lattice Boltzmann study of miscible viscous fingering for binary and ternary mixtures, *Phys. Rev. Fluids* **6**, 053904 (2021).
- [15] P. Jangir, R. Mohan, and P. Chokshi, Experimental study on the role of polymer addition in Saffman-Taylor instability in miscible flow displacement, *Phys. Fluids* **34**, 093102 (2022).
- [16] A. De Wit, Y. Bertho, and M. Martin, Viscous fingering of miscible slices, *Phys. Fluids* **17**, 054114 (2005).
- [17] T. K. Hota, S. Pramanik, and M. Mishra, Nonmodal linear stability analysis of miscible viscous fingering in porous media, *Phys. Rev. E* **92**, 053007 (2015).
- [18] V. Sharma, S. Pramanik, C.-Y. Chen, and M. Mishra, A numerical study on reaction-induced radial fingering instability, *J. Fluid Mech.* **862**, 624 (2019).
- [19] M. C. Kim, S. Pramanik, V. Sharma, and M. Mishra, Unstable miscible displacements in radial flow with chemical reactions, *J. Fluid Mech.* **917**, A25(2021).
- [20] S. Pramanik and M. Mishra, Effect of Péclet number on miscible rectilinear displacement in a Hele-Shaw cell, *Phys. Rev. E* **91**, 033006 (2015).
- [21] J. S. Nijjer, D. R. Hewitt, and J. A. Neufeld, The dynamics of miscible viscous fingering from onset to shutdown, *J. Fluid Mech.* **837**, 520 (2018).
- [22] B. S. Broyles, R. A. Shalliker, D. E. Cherrak, and G. Guiochon, Visualization of viscous fingering in chromatographic columns, *J. Chromatogr., A* **822**, 173 (1998).
- [23] R. A. Shalliker, B. S. Broyles, and G. Guiochon, Visualization of viscous fingering in high-performance liquid chromatographic columns: Influence of the header design, *J. Chromatogr. A* **865**, 73 (1999).
- [24] T. Suekane, J. Ono, A. Hyodo, and Y. Nagatsu, Three-dimensional viscous fingering of miscible fluids in porous media, *Phys. Rev. Fluids* **2**, 103902 (2017).
- [25] G. Rousseaux, A. De Wit, and M. Martin, Viscous fingering in packed chromatographic columns: Linear stability analysis, *J. Chromatogr. A* **1149**, 254 (2007).
- [26] C.-Y. Chen and E. Meiburg, Miscible displacements in capillary tubes. Part 2. Numerical simulations, *J. Fluid Mech.* **326**, 57 (1996).
- [27] C.-Y. Chen and E. Meiburg, Miscible displacements in capillary tubes: Influence of Korteweg stresses and divergence effects, *Phys. Fluids* **14**, 2052 (2002).

- [28] R. A. Wooding, The stability of a viscous liquid in a vertical tube containing porous material, [Proc. R. Soc. London A](#) **252**, 120 (1959).
- [29] M. A. Al-Gwaiz, *Sturm-Liouville Theory and its Applications*, Vol. 7 (Springer, New York, 2008).
- [30] A. Selim and D. A. S. Rees, The stability of a developing thermal front in a porous medium. I Linear theory, [J. Porous Media](#) **10**, 1 (2007).